Research Article | Open Access

Chemical Synthesis

Huang *et al. Chem. Synth.* **2026**, *6*, 46 **DOI:**10.20517/cs.2024.172

Defective graphene synergizes with NiO_x nanosheets to facilitate dual-defect-assisted two-electron oxygen reduction

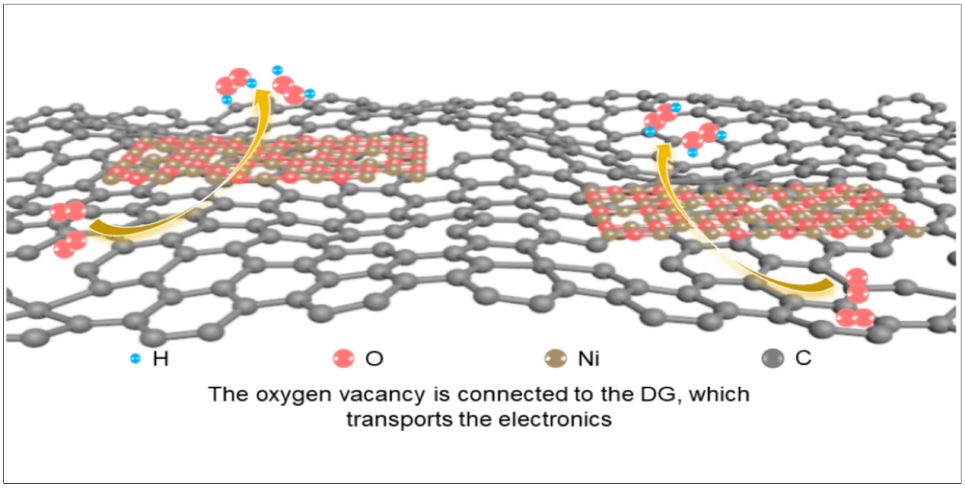
Run Huang[1], Helong Wu[1], Qingchao Fang[2], Ying Chen[1], Panjie Guo[1], Xuan Liu[1], Mengting Huang[1], Jinyan Zhang[1], Aijun Du[2], Lei Wang[1,*], Xin Wang[1,*]

Keywords:
NiO_x@DG, oxygen reduction reactions, hydrogen peroxide, electrocatalysis

Citation: Huang, R.; Wu, H.; Fang, Q.; Chen, Y.; Guo, P.; Liu, X.; Huang, M.; Zhang, J.; Du, A.; Wang, L.; Wang, X. Defective graphene synergizes with NiO_x nanosheets to facilitate dual-defect-assisted two-electron oxygen reduction. *Chem. Synth.* **2026**, *6*, 46. https://dx.doi.org/10.20517/cs.2024.172

Received: 13 Nov 2024 **First Decision:** 14 Dec 2024 **Revised:** 11 Jan 2025 **Accepted:** 22 Jan 2025 **Published:** 28 Apr 2026

Academic Editors: Ying Wan, Xiaoxin Zou **Copy Editor:** Ting-Ting Hu **Production Editor:** Ting-Ting Hu



Abstract

One of the biggest challenges in the electrochemical synthesis of H_2O_2 is the development of high-performance and economical catalysts. In this work, a two-dimensional composite material consisting of NiO_x nanosheets and defective graphene (DG) (NiO_x@DG) was prepared and showed excellent electrocatalytic performance toward electrosynthesis of H_2O_2 from oxygen reduction reaction. Particularly, the NiO_x@DG catalysts present superior activity indicators to physical mixing counterparts (NiO_x-DG), encompassing a high onset potential of 0.78 V, high efficiency and $2e^-$ selectivity over a wide potential range between 0.20-0.60 V (maximal value of 95%). The high activity of NiO_x@DG can be attributed to the dual-defects (oxygen vacancies on NiO_x and topological defects on DG)-induced strong electronic metal–support interaction. Such multi-defects collaborative enhancement strategy may provide a promising avenue for the preparation of high-performance catalysts toward application in different reactions.

Check for updates

[1]College of Chemical Engineering, Zhejiang University of Technology, Hangzhou 310032, Zhejiang, China.
[2]School of Chemistry, Physics and Mechanical Engineering Queensland University of Technology Brisbane, Brisbane 4000, Australia.

***Correspondence to:** Prof. Lei Wang, Prof. Xin Wang, College of Chemical Engineering, Zhejiang University of Technology, Hangzhou 310032, Zhejiang, China. E-mail: sumin224@zjut.edu.cn; wangxin136@zjut.edu.cn

INTRODUCTION

As an environmentally friendly and multipurpose oxidant, H_2O_2 is crucial to modern industry and is widely used in various fields including bleaching, textiles, chemical synthesis, wastewater treatment and disinfection[1,2]. Due to the inherent properties of H_2O_2, such as low cost, strong oxidizing tendency, the ability to eradicate pathogenic organisms, and the production of ecologically friendly byproducts of oxygen and water, traditional H_2O_2 wastewater recovery technologies provide ideal recovery efficiency. At present, the anthraquinone process produces about 95% of H_2O_2, but it comes with a high initial infrastructure cost, much energy input, a lot of byproducts, and significant safety risks when it comes to storing and transporting high concentrations of H_2O_2[3]. The electrochemical two-electron oxygen reduction reaction ($2e^-$ ORR) technology has recently served as a promising alternative pathway and has attracted enormous attention[4]. The key issue involving this route is the design of catalyst materials which need to convert traditional $4e^-$ ORR to $2e^-$ pathways[5]. Although a great number of catalysts, including precious metals[6-8], non-precious metals[9,10], metal oxides[11], carbon and its composite materials[3,12,13], have been developed and reported, their selectivity and activity are still far from practical utilization. Therefore, it is urgently required to explore new sustainable high-performance catalyst materials.

Currently, metal oxides are widely used in reactions such as OER, but they are not yet mature for $2e^-$ ORR. However, reasonable modification of them can greatly enhance the catalytic performance of non-precious metal oxides, even rivaling that of precious metal catalysts[14]. For example, amorphous materials are one such type. Recently, it has been found that some amorphous nanomaterials, including metal oxides, layered double hydroxides, and spinel compounds, exhibit high activity for electrochemical reactions due to their tunable composition, homogeneity, lattice defect-induced active sites, and unsaturated coordination active sites[15-17]. Moreover, under potentials where electrical conductivity is not dominant, amorphous metal oxides exhibit higher electrocatalytic activity for the oxygen evolution reaction (OER) compared to crystalline metal oxides[18-20]. This is because they are isotropic and single-phase, and unsaturated cation sites with more coordination are available for the reaction[21]. Although early results suggest that there is very little research on amorphous metal oxides as $2e^-$ ORR catalysts, the potential for amorphous materials to become competitive catalysts remains.

Carbon materials possess the advantages of high abundance, low cost, and strong electroreduction activity, along with tunable physicochemical properties and outstanding stability in corrosive acids. Heteroatom doping and intrinsic defects can be used to modify the electrical characteristics of carbon-based materials, which are intimately linked to their electrocatalytic activity and selectivity. For example, doping heteroatoms (N, S, B, P, *etc.*) into the carbon carriers has been shown to increase catalytic activity by inducing a local electronic structural rearrangement because of their distinct radii and electronegativities[22-26]. Additionally, the electrical neutrality of the conventional planar hexagonal graphite lattice can be broken by structural defects in carbon-based matrices, leading to asymmetric local electron redistribution. This greatly improves the electrocatalytic performance of non-metallic carbon materials[27-30]. Crucially, the neutral binding of the intermediate $^*OOH$ is a major determinant of both activity and selectivity. The adsorption energy of $^*OOH$ ($\Delta G_{^*OOH}$) may be optimized by amorphous catalysts with a large number of defect sites and disordered structures under thermodynamic equilibrium potentials[31]. Therefore, we expect that a combination of oxygen-deficient metal oxides and defective carbon materials may vary the local interfacial electronic properties via the dual-defect engineering to boost the $2e^-$ ORR performance.

In this work, we report the synthesis of oxygen-deficient NiO_x nanosheets (NiO_x NS) constructed at low temperatures and hydrothermally combined with defective graphene (DG), forming a synergistic effect between oxygen vacancies and defective topology. During this process, electrons from the defective topology flow through the oxygen vacancies to the Ni center, modulating the charge density at the Ni sites in the

reaction system and facilitating the electrochemical synthesis of H_2O_2. This further highlights the significant potential of defect engineering in carbon-supported oxides for electrochemical conversion applications.

EXPERIMENTAL

Materials and synthesis methods

Every reagent was acquired from commercial sources and used as received without extra purification. Nafion (5%), Potassium nitrate (KNO_3, AR) and Melamine ($C_3H_6N_6$, 99%) were purchased from Aladdin. Potassium hydroxide (KOH, ≥ 85%) was purchased from Titan Technology. Nickel acetylacetone ($C_{10}H_{14}NiO_4$, 98%) was purchased from Merrier Biochemical Technology. Single-layer graphene powder (G, 0.8-1.2 nm) was purchased from Jiangsu Xianfeng Nano Material Technology. Anhydrous ethanol [anhydrous ethanol(C_2H_5OH)] was obtained from Sinopharm Chemical.

Preparation of NiO_x nanosheet

Dissolve 30 mg of nickel acetylacetonate ($C_{10}H_{14}NiO_4$) and 60 mg of potassium nitrate in a mixed solution of deionized water and ethanol (V ethanol: V water = 5:1). After ultrasonication for one hour, evaporate the solvent to obtain the precursor. Place the precursor in a crucible and put it in a muffle furnace, heating at a rate of 5 °C·min^{-1} in air from room temperature to 350 °C, and hold for 1.5 h to obtain NiOx powder. Take a certain amount of NiO_x powder in a 50 mL centrifuge tube, add 30 mL of ethanol, and sonicate for 8 h. After centrifugation at 3,000 rpm, collect the supernatant as the NiO_x NS dispersion.

Preparation of DG

Uniformly mix 30 mg of G with 30 mg of melamine and place the mixture on a porcelain boat. Under a nitrogen (N_2) atmosphere, heat the mixture at a rate of 5 °C·min^{-1} from room temperature to 700 °C, and hold for 2 h; then, under the same atmosphere, increase the temperature at a rate of 5 °C·min^{-1} from 700 to 1,150 °C, hold for another 2 h, and allow the sample to cool to room temperature to obtain DG.

Take an appropriate amount of the prepared DG and disperse it in water to make a mixed solution with a concentration of 0.1 mg·mL^{-1}. Sonicate the solution for 8 h to obtain the DG dispersion.

Preparation of Nitrogen-doped graphene (NG)

Uniformly mix 30 mg of G with 30 mg of melamine and place the mixture on a porcelain boat. Under a N_2 atmosphere, heat the mixture at a rate of 5 °C·min^{-1} from room temperature to 700 °C, and hold for 2 h.

Preparation of NiO_x@DG

Mix the prepared NiOx dispersion with the DG dispersion in mass ratios of 6:1 and 9:1 for NiO_x to DG, respectively, under ultrasonication. Place the mixture in a 50 mL polytetrafluoroethylene (PTFE)-lined autoclave and hydrothermally treat at 60 °C for 12 h. Allow the product to cool down to room temperature after the treatment.

Preparation of NiO nanosheet

The synthesis method is similar to the aforementioned method for NiO_x, with the only difference being the absence of KNO_3.

Preparation of NiO_x NS-550

The synthesis method is similar to the aforementioned method for NiO_x, with the only difference being the temperature of 550 °C.

Preparation of NiO_x-DG

The synthesis method is similar to the aforementioned method for NiO_x@DG, with the only difference being the physical mixing.

Preparation of NiO_x@NG, NiO_x@G, NiO@DG, NiO@NG and NiO@G

The synthesis method is similar to the aforementioned method for NiO_x@DG, with the only difference being the hydrothermal treatment with the corresponding substance.

Materials characterizations

A Zeiss Geminisem 500 (Carl Zeiss AG, Germany) microscope operating at 5 kV was used to acquire scanning electron microscopy (SEM) pictures. Energy dispersive X-ray spectroscopy (EDX) mapping pictures, high-resolution transmission electron microscopy (HRTEM), high angle annular dark field scanning transmission electron microscopy (TEM), and TEM were acquired on the JEOL JEM-2100F (JEOL Ltd., Japan) 300 kV. The Rigaku Ultima IV (JEOL Ltd., Japan) was used to record X-ray diffraction (XRD) patterns. It operated at 40 kV with Cu Kα radiation (λ = 0.15406 nm), a scan rate of 10°/min, and a theta range of 5° to 90°. Raman spectra were obtained using a laser with a wavelength of 532 nm on a Raman spectrometer system (Raman spectrometer model: HORIBA HR Evolution, HORIBA, Ltd., France). The Brunauer-Emmett-Teller (BET) surface area of +the resultant materialthe resultant materialthe resultant material was calculated using a relative pressure of P/P_0 = 0.05-0.1. An Al-Ka radiation-powered Thermo Scientific K-Alpha device (Thermo Fisher Scientific, America) operating at 12 kV was used to perform X-ray photoelectron spectroscopy (XPS). The beamline 4B9A at the Beijing Synchrotron Radiation Facility (BSRF) in Beijing, China, has an optical emission end station where the Ni-K-edge X-ray absorption near-edge structure (XANES) spectra of the catalysts were examined.

Electrochemical measurements

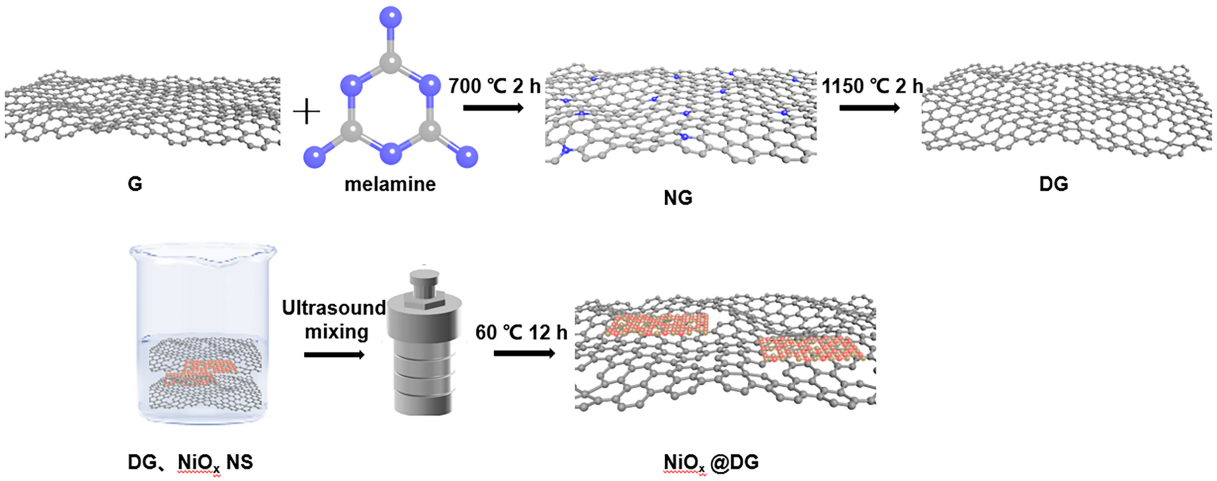
Through the use of the CHI760E electrochemical workstation, a three-electrode system is used for all electrochemical testing. An Ag/AgCl electrode (saturated KCl solution), a carbon rod, and a rotating ring disc electrode (RRDE) (glassy carbon disc, 4 mm diameter, 5 mm inner diameter, 7 mm outer diameter, Pt ring) make up a three-electrode system. The platinum wire was used as the counter electrode and the Ag/AgCl electrode was used as the reference electrode. The reversible hydrogen electrode (RHE), $E_{RHE} = E_{Ag/AgCl} + 0.197 + 0.0592^{*}PH$[32], was used to calibrate the reference electrode. Materials 5 mg of the sample, 10 uL of Nafion (5 weight percent), 700 uL of water, and 290 uL of isopropanol were sonicated for 1 h to create catalyst ink. The disc electrode was then covered with 5 uL of the dispersion, which was allowed to dry at room temperature. At the disc electrode, the catalyst's mass loading was 0.20 $mg{\cdot}cm^{-2}$. Before testing, O_2 was passed into 0.1 M KOH for 30 min to make sure O_2 saturation was achieved. Linear scanning voltammetry (LSV) tests were performed at 1,600 rpm in an O_2-saturated 0.1 M KOH electrolyte. Repeat at a scan rate of 10 $mV{\cdot}s^{-1}$ over a potential range of 0.1 V *vs*. RHE to 1.0 V *vs*. RHE. The ring potential was also held at 1.2 V *vs*. RHE. Normalize all current densities to the area of the disc electrode.

The hydrogen peroxide yield [H_2O_2 (%)] and the number of electron transfers (n) are calculated based on[33]

$$n = 4 \times \frac{I_d}{I_{d+I_r/N}} \quad (1)$$

$$H_2O_2(\%) = 200 \times \frac{I_r/N}{I_d + I_r/N} \quad (2)$$

Where I_d represents the disk current, I_r denotes the ring current, and N = 0.42 signifies the current collection efficiency of the platinum ring.



Scheme 1. The schematic procedure for synthesizing the NiO_x@DG; The gray balls represent C, the blue balls represent N, the red balls represent Ni, and the brown balls represent O. DG: Defective graphene; NG: nitrogen-doped graphene.

RESULTS AND DISCUSSION

Morphology and structure

NiO_x@DG was synthesized following the procedure depicted in Scheme 1, and detailed information can be found in the Supporting Information. In simple terms, NiO_x powder was obtained by heating nickel acetylacetone and KNO_3 in a muffle furnace at 350 °C for 90 min. In the XRD result [Supplementary Figure 1], it was concluded from the observation of characteristic peaks that the XRD of bulk NiO_x showed the characteristic peaks of NiO. This was because KNO_3 can act as an oxidizing base in this process, providing O^{2-} to form metal oxides[34]. Furthermore, it was evident that the characteristic peaks of NiO_x bulk are broader and lower compared to those of NiO. This was attributed to the introduction of oxygen vacancies, which disrupt the order of the oxide's lattice structure. In the SEM images [Supplementary Figure 2A], we can observe its rough surface, and the layered structure can be clearly seen (indicated by the white arrows in the image). However, no distinct particles were observed in the TEM images [Supplementary Figure 2B]. Nevertheless, HRTEM further describes the morphological structure of the NiO_x powder and the spatial distribution of the NiO particles within it. The presence of small black particles as NiO is indicated [enclosed by red dashed lines in Supplementary Figure 2C], and the lattice fringe spacing of 0.244 nm corresponds to the interplanar spacing of the (111) plane of NiO [Supplementary Figure 2D-F], a result that was consistent with the XRD analysis. The elemental mapping results [Supplementary Figure 2G] showed that Ni and O elements were uniformly distributed on the surface of the carbon carrier. Subsequently, the NiO_x powder was placed in ethanol and sonicated to exfoliate NiO_x NS, and the upper clear liquid was taken to remove larger NiO crystal particles and incompletely exfoliated bulk NiO_x. This was followed by hydrothermal treatment with DG (for detailed procedures, see Supporting Information) to obtain the final NiO_x@DG composite. In addition, control samples, including physical mixtures of NiO_x and DG (NiO_x-DG) and NiO_x@DG-9 composite with a changed mass ratio (NiO_x:DG = 9:1), were also prepared.

We characterized the composited sample to confirm the completion of exfoliation. From the XRD image in [Supplementary Figure 3], it can be observed that the characteristic peaks of the oxides disappear after the exfoliation and composite process. This indicated that centrifugation can separate the big crystalline particles and bulk NiO_x, leaving behind NiO_x NS in the upper clear liquid. In the SEM image [Figure 1A], NiO_x NS with a diameter of approximately 100 nm can be observed loaded on DG, and the presence of these nanosheets was also observed in the TEM image [Figure 1B]. The average thickness of NiO_x@DG was measured to be about 2 nm using atomic force microscopy (AFM) [Figure 1C and D]. HRTEM and

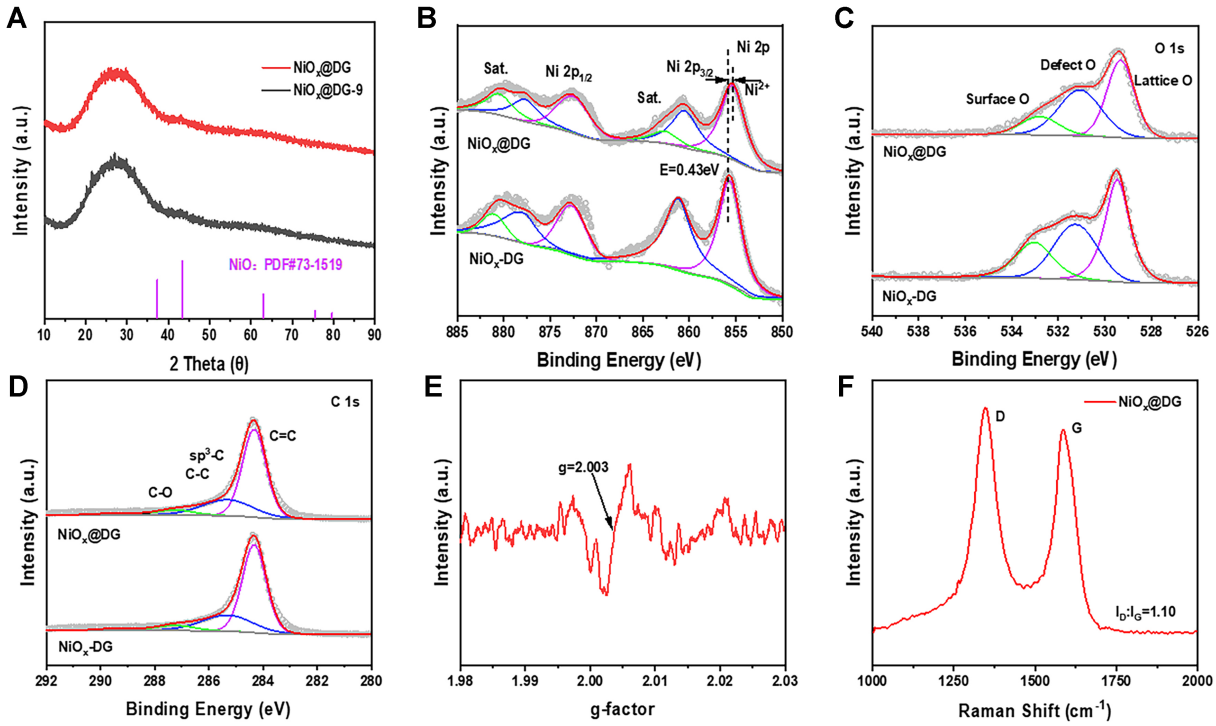


Figure 1. (A) SEM image, (B) TEM image, (C) AFM image of NiO_x@DG and (D), Height profile along the line of NiO_x@DG; (E) HRTEM image and (F) The enlarged HRTEM image within the red dashed frame marks the local area of disordered atoms; (G and H) SEM and line-scan element mapping for NiO_x@DG. SEM: Scanning electron microscopy; TEM: transmission electron microscopy; AFM: atomic force microscopy; DG: defective graphene; HRTEM: high-resolution transmission electron microscopy.

corresponding inverse fast Fourier transform (IFFT) images were used to investigate the presence of crystalline structures of NiO [Figure 1E and F and Supplementary Figure 4]. In specific areas (enclosed by red boxes), irregular atomic arrangements were observed, indicating the presence of characteristic features of defective structures, which was caused by the overflow of lattice oxygen, consistent with the XRD results. Line scan analysis and elemental mapping spectra revealed the uniform distribution of C, O and Ni over the composite catalysts [Figure 1G and H and Supplementary Figure 5].

The powder XRD (PXRD) patterns [Figure 2A] verified that no clear typical diffraction peaks of metal oxides were present in NiO_x@DG and NiO_x@DG-9, with the exception of a broad peak at about 26° corresponding to the (002) plane of graphitic carbon. Subsequently, the chemical properties of the samples were thoroughly investigated using XPS. The high-resolution XPS spectra of Ni 2p for NiO_x@DG and NiO_x-DG are shown in Figure 2B and Supplementary Figure 6. These spectra can be well-deconvoluted into several sub-peaks that correspond to Ni2+ (nearly 855.7 eV) and two associated satellite peaks. Compared to NiO_x-DG, there is a noticeable negative shift of around 0.45 eV in the Ni2+ peak of NiO_x@DG, indicating that Ni acts as an electron acceptor to receive electrons transferred from DG. However, there is no significant shift in the Ni 2p XPS spectra between NiO_x NS-350 and NiO_x-DG [Supplementary Figure 7], implying that simple physical mixing cannot alter the electronic structure of the Ni centers. The Ni 2p XPS spectrum of NiO_x@DG-9 also shows two peaks [Supplementary Figure 8], the oxidation peak of Ni (2+) at a binding energy of ~ 855.7 eV, and the associated satellite peak, which is consistent with the results of Ni oxides observed in XRD and HRTEM. A larger negative shift in binding energy of 0.8 eV can be observed, suggesting that higher loading of NiO_x NS in NiO_x@DG-9 is beneficial for more oxygen vacancies to communicate with DG, thereby gaining more electrons. In the high-resolution XPS spectrum of O 1s [Figure 2C], three peaks can be observed, which were assigned to lattice oxygen at 529.93 eV, surface adsorbed oxygen at 532.63 eV, and

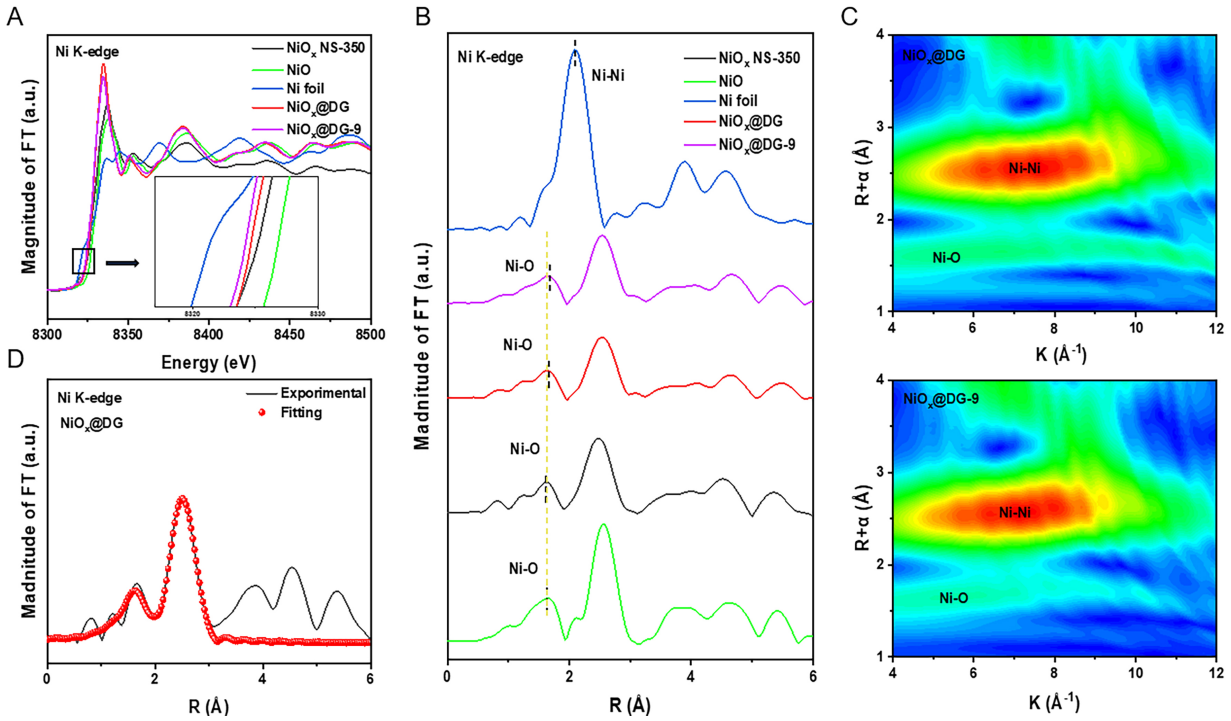


Figure 2. (A) PXRD patterns; (B) Ni 2p XPS spectra; (C) N 1s XPS spectra and (D) C 1s XPS spectra of NiO_x@DG and NiO_x-DG; (E) EPR spectra of NiO_x@DG; (F) Raman spectroscopy of NiO_x@DG. PXRD: Powder X-ray diffraction; XPS: X-ray photoelectron spectroscopy; DG: defective graphene.

lattice oxygen near oxygen vacancies at 531.4 eV. The O_d/O_t (O_d represents oxygen vacancy content and O_t indicates the total O content) ratio of NiO_x@DG was 20%, lower than that of NiO_x-DG (36.5%), which may be attributed to the increased surface adsorbed oxygen during the hydrothermal treatment to synthesize NiO_x@DG composite[35]. Figure 2D showed the high-resolution XPS spectra of C 1s, which can be deconvoluted into three subpeaks, corresponding to C=C (sp^2 carbon, 284.6 eV), C-C (sp^3 carbon, 285.3 eV), and C-O (287.3 eV). The electron paramagnetic resonance (EPR) results also confirmed the presence of oxygen vacancies, with a characteristic peak at g = 2.003, which was attributed to the formation of trapped electrons by oxygen vacancies [Figure 2E][36]. Moreover, it has been reported that oxygen vacancies play a role in enhancing the ORR activity[37]. This further illustrates that KNO_3 was essential for the low-temperature construction of amorphous oxides [Supplementary Figure 9]. According to the reports, the electron transfer from the carrier to the active center also involves the synergistic participation of oxygen vacancies (The following text discusses in detail)[38]. The I_D:I_G = 1.10 in the Raman spectrum further indicated that DG had a large number of defects [Figure 2F and Supplementary Figure 10].

Extended X-ray absorption fine structure (EXAFS) and XANES studies were performed to further determine the local coordination environment of Ni in the catalyst. The Ni-K edge XANES spectra for the NiO_x@DG and reference materials are shown in Figure 3A. The absorption edges of these samples were located between the absorption edge of Ni foil and NiO. The Ni valence state was between 0 and +2, which was consistent with the XPS data. The Fourier-transformed EXAFS curves for NiO_x@DG, NiO_x@DG-9, and NiO_x NS-350 also showed the presence of Ni-O, with a peak in the R-space at approximately 1.68 Å, confirming that the Ni species primarily exist in the form of NiO clusters [Figure 3B]. The intensity of the peak is related to the number of atoms with the same average interatomic distance and the distribution of Ni centers[39]. The introduction of oxygen vacancies led to the reduction of central Ni species, resulting in a decrease in coordination number and an increase in bond length compared to NiO, which was consistent with other

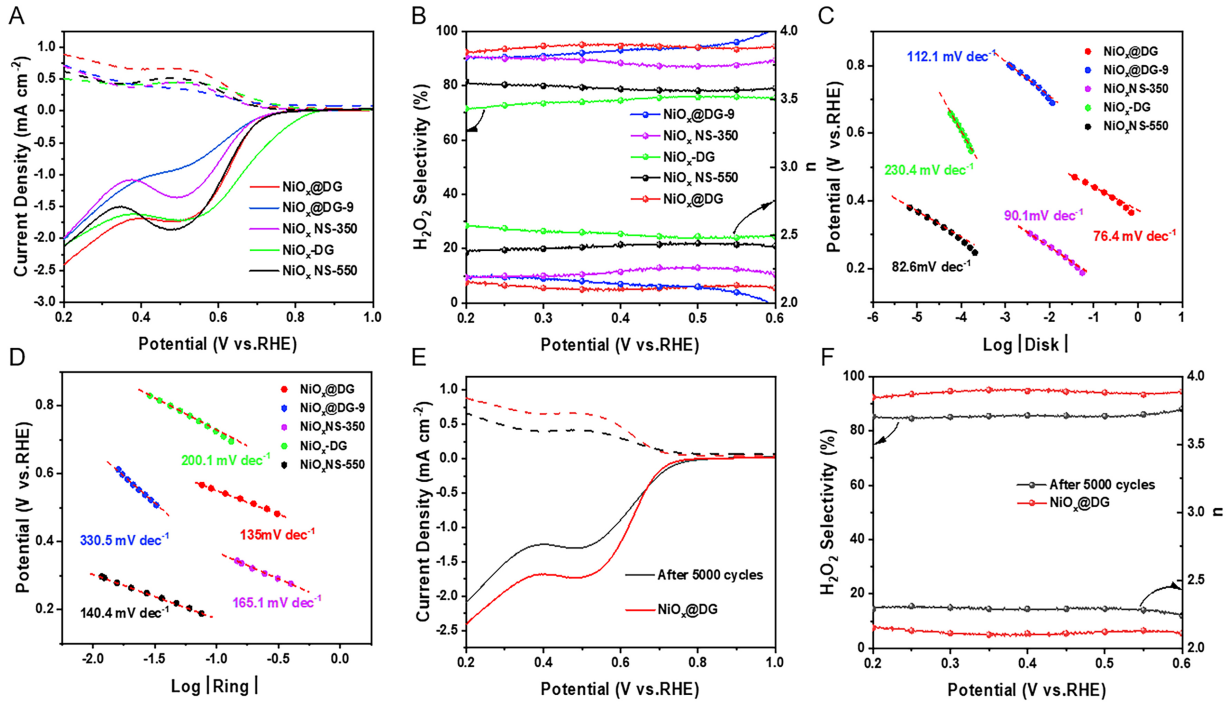


Figure 3. (A) Normalized Ni K-edge XANES spectra of NiO_x@DG and reference materials; (B) FT of Ni K-edge EXAFS data of NiO_x@DG and reference materials. The boxed area is enlarged in Figure 3A's inset; (C) Ni K-edge WT-EXAFS contour plots for NiO_x@DG and reference materials; (D) Ni K-edge EXAFS fitting curves for NiO_x@DG. XANES: X-ray absorption near-edge structure; DG: defective graphene; FT: fourier transform; EXAFS: extended X-ray absorption fine structure; WT: wavelet transform.

literature reports[40]. There is no Ni-Ni scattering channel at ~ 2.2 Å that corresponds to the crystal nickel metal structure. In the meantime, the Ni-O_{xo} backward scattering path of NiO is closely matched by another prominent peak at about 2.6 Å[41]. The wavelet transform (WT)-EXAFS method can be used to distinguish backscattered atoms in R space and K space. Figure 3C and Supplementary Figure 11 demonstrated that the WT contour plots of the various reference samples show Ni-O at ~ 5.0 $Å^{-1}$; the intensity of Ni-O is strongest at ~ 7.3 $Å^{-1}$ in WT contour plots of different prepared samples, which corresponds to the Ni-Ni coordination structure of NiO and further indicates the presence of NiO_x. Finally, in order to accurately determine the local coordination environment of the Ni species, quantitative EXAFS fitting was carried out. The fitting results in Figure 3D and Supplementary Table 1 show that the Ni-O coordination number in NiO_x@DG is approximately 4.46, less than the Ni-O coordination number of bulk NiO (6.0). This result confirms the existence of oxygen vacancies.

Performance testing

RRDE on a three-electrode system was used to assess the ORR performance of the catalysts in 0.1 M KOH solution. We first studied the effect of catalyst loading amount on ORR activity. As shown in Supplementary Figure 12, the optimal catalytic performance can be achieved when the loading amount is below 0.2 $mg·cm^{-2}$. The decrease in activity of high loading amounts may be attributed to a more severe catalyst stacking effect, which weakens the wettability and accessibility to the electrolyte. When the electrode loading is as low as 0.1 $mg·cm^{-2}$, although high $2e^-$ ORR acticity is preserved, systematic errors are inevitably introduced during the measurement process. Therefore, we choose 0.2 $mg·cm^{-2}$ as the testing loading amount for all the materials. The linear sweep voltammetry (LSV) curves in Figure 4A reveal that the disk-limited current density of NiO_x@DG exceeds all the other tested samples, with the value of about 2.4 $mA·cm^{-2}$ close to the theoretical mass transfer limit for the $2e^-$ ORR process (~ 3 $mA·cm^{-2}$)[7,42]. For NiO_x@DG, NiO_x@DG-9, NiO_x NS-350, and NiO_x NS-550, the onset potential (defined as the potential at a current density of 0.1 $mA·cm^{-2}$)

was all about 0.78 V, almost greater than the thermodynamic limit of 0.76 V (pH = 13 in 0.1 M KOH). Previous studies have shown that a potential related to the Nernst effect, exceeding the limit, can arise due to a combination of high $2e^-$ ORR catalytic activity and a low concentration of H_2O_2 generated in an alkaline environment[10,43,44]. For NiO_x-DG, the higher onset potential (0.86 V), the higher disk current density (~ 2.1 $mA{\cdot}cm^{-2}$), and the lower ring current density (~ 0.5 $mA{\cdot}cm^{-2}$) indicated that they favor the kinetics of the $4e^-$ ORR pathway. According to Figure 4B, the $2e^-$ route consumes most of the electrons for NiO_x@DG throughout a broad potential range, offering a high H_2O_2 selectivity of almost 95% and an electron transfer number that is closest to 2 (2.1). This overwhelmed many reported catalysts for the electric production of H_2O_2 [Supplementary Table 2]. In contrast, NiO_x-DG obtained through physical mixing only has about 75% H_2O_2 selectivity, with an electron transfer number of n = 2.5. This was attributed to the difficulty in the physical mixing process for the electron cloud density of DG defects to be transported through oxygen vacancies as an electron bridge, resulting in a lower electron cloud density at the Ni sites. The high electron cloud density at the centers of activity sites was essential for the adsorption and desorption of intermediates[45]. The rate-determining step (RDS) and reaction kinetics were analyzed using the Tafel slopes [Figure 4C]. The disk Tafel slopes for the various samples were 230.4 $mV{\cdot}dec^{-1}$ (NiO_x-DG), 112.1 $mV{\cdot}dec^{-1}$ (NiO_x@DG-9), 90.1 $mV{\cdot}dec^{-1}$ (NiO_x NS-350), 82.6 $mV{\cdot}dec^{-1}$ (NiO_x NS-550), and 76.4 $mV{\cdot}dec^{-1}$ (NiO_x@DG), verifying that the RDS changed from the first $^*OOH$ production stage ($O_2 \rightarrow {}^*OOH$, ~ 120 $mV{\cdot}dec^{-1}$) to the dissociation step ($^*OOH \rightarrow H_2O_2$, ~ 70 $mV{\cdot}dec^{-1}$)[46,47]. Additionally, the NiO_x@DG sample exhibited the lowest Tafel slope for the ring current, indicating its capability for rapid H_2O_2 production [Figure 4D]. This was likely due to the oxygen vacancies acting as electron bridges, leading to a higher electron density at the Ni sites, which was relevant to the adsorption/desorption of intermediates[48]. Accelerated deterioration tests (ADT) were subsequently used to assess the catalyst's stability, as shown in Figure 4E and F. The outstanding endurance of NiO_x@DG for the electrosynthesis of H_2O_2 was confirmed by the LSV curves, which showed a negative shift after 5,000 ADT cycles but still maintained a high H_2O_2 selectivity of about 85%. For the chronoamperometry stability test at a constant potential of 0.2 V *vs*. RHE, the ring-disk current slowly decreases as ORR proceeds, but the selectivity is maintained at a relatively high level of 86%, which can be comparable with many reported excellent catalysts toward $2e^-$ ORR [Supplementary Figure 13 and Supplementary Table 3]. To investigate the reason for activity deterioration after cyclic voltammetry (CV) stability testing, we conducted series of post-mortem characterizations [Supplementary Figure 14]. According to the HRTEM images, distinct NiO lattice fringes can be observed, indicating most NiO crystal is preserved. However, extensive defect structures emerge in the NiO lattice. This confirms that lixiviation of Ni species occurs during the CV stability testing. The dissolution of partial Ni sites can also be demonstrated by the XPS spectra and inductively coupled plasma mass spectrometry (ICP-MS) data [Supplementary Table 4]. All these findings affirm that the activity decrease of NiO_x@DG during long-term working conditions comes from the slow Ni leaching into the electrolytes.

To further confirm the synergistic effect of oxygen vacancies in NiO_x and topological defects in DG for the electrosynthesis of hydrogen peroxide, two single-defect samples (NiO_x@G and NiO@DG) were prepared for comparison. As illustrated in Supplementary Figures 15 and 16, both NiO_x@G and NiO@DG manifested significantly reduced H_2O_2 selectivity compared with NiO_x@DG composites, emphasizing the critical role of synergy between interfacial oxygen vacancies and carbon defects toward $2e^-$ ORR. Noteworthily, the ORR pathway on the NiO@DG sample is $4e^-$ process, while NiO_x@G still preserves certain electrosynthesis performance of H_2O_2. In addition, comparing the ORR performance between NiO@DG and NiO@G [Supplementary Figure 17] also confirms that only introducing intrinsic carbon defects in G cannot activate the Ni atoms in hybridized NiO materials. All the results demonstrate the dual defects promoted mechanism in NiO_x@DG can be depicted as follows: (1) Oxygen vacancies play a crucial role in activating the adjacent Ni atoms to serve as the main active centers, transferring $4e^-$ ORR route to approach $2e^-$ pathway; (2) The coupled topological defects in DG possibly optimize the electronic structures around active sites, finally attaining an optimal electrocatalytic performance toward $2e^-$ ORR.

Doping heteroatoms in carbon materials is also well-accepted to efficiently regulate the atomic and electronic configurations besides the intrinsic defect engineering. Hence, we further studied whether doping N_2 atoms in G can also boost the H_2O_2 electroproduction performance, similar to the effect of topological defects. As shown in Supplementary Figures 18 and 19, N dopants in G cannot lead to activity enhancement in $2e^-$ ORR as compared to NiO@G and NiO_x@G, which indicates its uselessness in such composite system toward ORR process. To directly uncover the influence of the G substrate itself on ORR processes, a series of G-based carbon materials were prepared with similar methods at different temperatures (800-1,150 °C, denoted as NG-800, NG-900, NG-1,000 and DG-1,150 °C) were prepared. The defect structure and elemental state were first characterized by Raman and XPS spectra, showing that N_2 content decreased while the defect density rose as the pyrolysis temperature increased, consistent with previous reports that removal of N_2 dopants in carbon lattice can induce the rearrangement of surrounding carbon atoms to form more topological defects [Supplementary Figure 20A and B]. The ORR activities of these carbon samples were then evaluated on RRDE and the results were presented in Supplementary Figure 20C and D. Apparently, the ORR processes on all the carbon materials without coupled NiO species are close to $4e^-$ transfer pathway, indicating that neither N dopants nor carbon defects can directly boost the desorption of generated H_2O_2 to prevent the cleavage of O-O bonds. This can further confirm our speculation that, in NiO_x@DG composites, Ni atoms beside oxygen vacancies act as the real catalytic centers for O_2 adsorption and activation, while the interfacial carbon defects contribute to optimizing the electronic structure of active Ni atom to achieve the final excellent $2e^-$ ORR activity.

Density functional theory (DFT) calculations were further conducted to gain a deep understanding on the activity mechanism. As pentagon defects in carbon lattice have been demonstrated to show excellent electrocatalytic performance in various reactions, here we choose G lattice possessing pentagon defects as the defective carbon model. Accordingly, three composite models were constructed: NiO with one oxygen vacancy coupled DG (NiO_x@DG) [Supplementary Figure 21A], NiO with one oxygen vacancy coupled perfect G (NiO_x@G) [Supplementary Figure 21B], and NiO lattice without oxygen vacancies coupled DG (NiO@DG) [Supplementary Figure 21C]. The models with adsorbed $^*OOH$ intermediates were also presented in Supplementary Figure 21. It can be seen that, only in NiO_x@DG model, the $^*OOH$ is laterally adsorbed on the NiO_x layer, which may facilitate the elongation of the O–O bond[16], and lead to the consequent desorption process. The adsorption energy of the key intermediate $^*OOH$ is generally used as a key descriptor for predicting the $2e^-$ ORR.[15] As shown in Supplementary Figure 21D, NiO_x@DG model has the lowest energy barrier (1.24 eV) under alkaline conditions as compared to the other two models, indicating its energetically favorable $2e^-$ ORR process due to the enhanced intermediate desorption capacity.

CONCLUSION

In summary, we prepared oxygen-deficient NiO_x using a low-temperature molten salt method and conducted a composite process with DG (NiO_x@DG). This not only enhanced the conductivity but also connected the DG to the Ni centers through oxygen vacancies, increasing the electron cloud density of Ni and improving the $2e^-$ ORR activity of the catalyst. The oxygen vacancies acted as a bridge for electron transport, facilitating the transfer from the topological defects of the DG to the Ni centers. The catalyst achieved a 95% selectivity for hydrogen peroxide under alkaline conditions, with a Tafel slope of 72.6 $mV \cdot dec^{-1}$. After 5,000 cycles of CV, the selectivity for hydrogen peroxide remained at 85%, demonstrating good stability.

DECLARATIONS

Acknowledgements

The authors would like to thank Shi-yanjia Lab (www.shiyanjia.com) for material characterizations and thank facility support of the 4B9A beamline of Beijing Synchrotron Radiation Facility (BSRF).

Authors' contributions

Conceptualization, investigation, methodology, data curation, formal analysis, DFT calculations, writing - original draft: Huang, R.; Wu, H.; Fang, Q.; Chen, Y.; Guo, P.; Liu, X.; Huang, M.; Zhang, J.; Du, A.
Conceptualization, funding acquisition, resources, supervision, project administration, writing - review and editing: Wang, L.; Wang, X.

Availability of data and materials

The authors confirm that the data supporting the findings of this study are available within its Supplementary Materials.

AI and AI-assisted tools statement

During the preparation of this manuscript, the AI tool Kimi (version Enterprise API, released online in China in August 2024) was used solely for language editing. The tool did not influence the study design, data collection, analysis, interpretation, or the scientific content of the work. All authors take full responsibility for the accuracy, integrity, and final content of the manuscript.

Financial support and sponsorship

This work was supported by the National Natural Science Foundation of China (NSFC, Nos. 22275165, 22101254, and 52403118).

Conflicts of interest

All authors declared that there are no conflicts of interest.

Ethical approval and consent to participate

Not applicable.

Consent for publication

Not applicable.

Copyright

© The Author(s) 2026.

Supplementary Materials

Supplementary Materials

REFERENCES

1. Jiang, Y.; Ni, P.; Chen, C.; et al. Selective electrochemical H_2O_2 production through two-electron oxygen electrochemistry. *Adv. Energy. Mater.* **2018**, *8*, 1801909. DOI
2. Sun, Y.; Han, L.; Strasser, P. A comparative perspective of electrochemical and photochemical approaches for catalytic H_2O_2 production. *Chem. Soc. Rev.* **2020**, *49*, 6605-31. DOI
3. Wu, Z.; Wang, T.; Zou, J.; Li, Y.; Zhang, C. Amorphous nickel oxides supported on carbon nanosheets as high-performance catalysts for electrochemical synthesis of hydrogen peroxide. *ACS. Catal.* **2022**, *12*, 5911-20. DOI
4. Tian, Q.; Jing, L.; Wang, W.; et al. Utilizing carbonaceous catalysts for H2O2 electrosynthesis via the two-electron oxygen reduction reaction. *Energy. Lab.* **2025**, *3*, 240019. DOI
5. Liu, W.; Zhang, C.; Zhang, J.; et al. Tuning the atomic configuration of Co-N-C electrocatalyst enables highly-selective H2O2 production in acidic media. *Appl. Catal. B. Environ.* **2022**, *310*, 121312. DOI
6. Jirkovský, J. S.; Panas, I.; Ahlberg, E.; Halasa, M.; Romani, S.; Schiffrin, D. J. Single atom hot-spots at Au-Pd nanoalloys for electrocatalytic H_2O_2 production. *J. Am. Chem. Soc.* **2011**, *133*, 19432-41. DOI PubMed

7. Siahrostami, S.; Verdaguer-Casadevall, A.; Karamad, M.; et al. Enabling direct H_2O_2 production through rational electrocatalyst design. *Nat. Mater.* **2013**, *12*, 1137-43. DOI PubMed
8. Ko, Y.; Choi, K.; Yang, B.; et al. A catalyst design for selective electrochemical reactions: direct production of hydrogen peroxide in advanced electrochemical oxidation. *J. Mater. Chem. A.* **2020**, *8*, 9859-70. DOI
9. Xie, J.; Zhong, L.; Yang, X.; et al. Phosphorous and selenium tuning Co-based non-precious catalysts for electrosynthesis of H_2O_2 in acidic media. *Chin. Chem. Lett.* **2024**, *35*, 108472. DOI
10. Jung, E.; Shin, H.; Lee, B. H.; et al. Atomic-level tuning of Co-N-C catalyst for high-performance electrochemical H_2O_2 production. *Nat. Mater.* **2020**, *19*, 436-42. DOI
11. Yan, L.; Cheng, X.; Wang, Y.; et al. Exsolved Co_3O_4 with tunable oxygen vacancies for electrocatalytic H_2O_2 production. *Mater. Today. Energy.* **2022**, *24*, 100931. DOI
12. Sun, Y.; Sinev, I.; Ju, W.; et al. Efficient electrochemical hydrogen peroxide production from molecular oxygen on nitrogen-doped mesoporous carbon catalysts. *ACS. Catal.* **2018**, *8*, 2844-56. DOI
13. Liu, Y.; Quan, X.; Fan, X.; Wang, H.; Chen, S. High-yield electrosynthesis of hydrogen peroxide from oxygen reduction by hierarchically porous carbon. *Angew. Chem.* **2015**, *127*, 6941-5. DOI
14. Wang, M.; Zhang, N.; Feng, Y.; Hu, Z.; Shao, Q.; Huang, X. Partially pyrolyzed binary metal-organic framework nanosheets for efficient electrochemical hydrogen peroxide synthesis. *Angew. Chem. Int. Ed. Engl.* **2020**, *59*, 14373-7. DOI
15. Cai, P.; Huang, J.; Chen, J.; Wen, Z. Oxygen-containing amorphous cobalt sulfide porous nanocubes as high-activity electrocatalysts for the oxygen evolution reaction in an alkaline/neutral medium. *Angew. Chem. Int. Ed. Engl.* **2017**, *56*, 4858-61. DOI
16. Indra, A.; Menezes, P. W.; Zaharieva, I.; et al. Active mixed-valent MnO_x water oxidation catalysts through partial oxidation (corrosion) of nanostructured MnO particles. *Angew. Chem. Int. Ed. Engl.* **2013**, *52*, 13206-10. DOI
17. Yin, S.; Tu, W.; Sheng, Y.; et al. A highly efficient oxygen evolution catalyst consisting of interconnected nickel-iron-layered double hydroxide and carbon nanodomains. *Adv. Mater.* **2018**, *30*, 1705106. DOI
18. Zhang, C.; Zhang, X.; Daly, K.; Berlinguette, C. P.; Trudel, S. Water oxidation catalysis: tuning the electrocatalytic properties of amorphous lanthanum cobaltite through calcium doping. *ACS. Catal.* **2017**, *7*, 6385-91. DOI
19. Smith, R. D.; Prévot, M. S.; Fagan, R. D.; et al. Photochemical route for accessing amorphous metal oxide materials for water oxidation catalysis. *Science* **2013**, *340*, 60-3. DOI PubMed
20. Pan, L.; Wang, Q.; Li, Y.; Zhang, C. Amorphous cobalt-cerium binary metal oxides as high performance electrocatalyst for oxygen evolution reaction. *J. Catal.* **2020**, *384*, 14-21. DOI
21. Li, X.; Cai, W.; Li, D.; Xu, J.; Tao, H.; Liu, B. Amorphous alloys for electrocatalysis: the significant role of the amorphous alloy structure. *Nano. Res.* **2023**, *16*, 4277-88. DOI
22. Xia, Y.; Zhao, X.; Xia, C.; et al. Highly active and selective oxygen reduction to H_2O_2 on boron-doped carbon for high production rates. *Nat. Commun.* **2021**, *12*, 24329. DOI PubMed PMC
23. Jiao, Y.; Zheng, Y.; Jaroniec, M.; Qiao, S. Z. Origin of the electrocatalytic oxygen reduction activity of graphene-based catalysts: a roadmap to achieve the best performance. *J. Am. Chem. Soc.* **2014**, *136*, 4394-403. DOI PubMed PMC
24. Chen, G.; Liu, J.; Li, Q.; et al. A direct H_2O_2 production based on hollow porous carbon sphere-sulfur nanocrystal composites by confinement effect as oxygen reduction electrocatalysts. *Nano. Res.* **2019**, *12*, 2614-22. DOI
25. Zhang, J.; Zhang, J.; He, F.; et al. Defect and doping Co-engineered non-metal nanocarbon ORR electrocatalyst. *Nanomicro. Lett.* **2021**, *13*, 65. DOI PubMed PMC
26. Melchionna, M.; Fornasiero, P.; Prato, M. The rise of hydrogen peroxide as the main product by metal-free catalysis in oxygen reductions. *Adv. Mater.* **2019**, *31*, 1802920. DOI
27. Chen, S.; Chen, Z.; Siahrostami, S.; et al. Defective carbon-based materials for the electrochemical synthesis of hydrogen peroxide. *ACS. Sustainable. Chem. Eng.* **2018**, *6*, 311-7. DOI
28. Zhang, L.; Xu, Q.; Niu, J.; Xia, Z. Role of lattice defects in catalytic activities of graphene clusters for fuel cells. *Phys. Chem. Chem. Phys.* **2015**, *17*, 16733-43. DOI PubMed
29. Zhu, J.; Huang, Y.; Mei, W.; et al. Effects of intrinsic pentagon defects on electrochemical reactivity of carbon nanomaterials. *Angew. Chem. Int. Ed.* **2019**, *58*, 3859-64. DOI PubMed
30. Wang, W.; Shang, L.; Chang, G.; et al. Intrinsic carbon-defect-driven electrocatalytic reduction of carbon dioxide. *Adv. Mater.* **2019**, *31*, e1808276. DOI PubMed
31. Huang, J.; Fu, C.; Chen, J.; Senthilkumar, N.; Peng, X.; Wen, Z. The enhancement of selectivity and activity for two-electron oxygen reduction reaction by tuned oxygen defects on amorphous hydroxide catalysts. *CCS. Chem.* **2022**, *4*, 566-83. DOI
32. Shen, S.; Jiang, J.; Guo, P.; et al. Effect of Cr doping on the photoelectrochemical performance of hematite nanorod photoanodes. *Nano. Energy.* **2012**, *1*, 732-41. DOI

33. Paulus, U. A.; Schmidt, T. J.; Gasteiger, H. A.; Behm, R. J. Oxygen reduction on a high-surface area Pt:Vulcan carbon catalyst: a thin-film rotating ring-disk electrode study. *J. Electroanal. Chem.* **2001**, *495*, 134-45. DOI
34. FLOOD, H.; FORLAND, T. The acidic and basic properties of oxides. *Acta. Chem. Scand.* **1947**, *1*, 592-604. DOI PubMed
35. Deming, C. P.; Mercado, R.; Gadiraju, V.; Sweeney, S. W.; Khan, M.; Chen, S. Graphene quantum dots-supported palladium nanoparticles for efficient electrocatalytic reduction of oxygen in alkaline media. *ACS. Sustainable. Chem. Eng.* **2015**, *3*, 3315-23. DOI
36. Liu, Q.; Zhu, Y.; He, Z.; Jin, S.; Chen, Y. A facile top-down approach for constructing perovskite oxide nanostructure with abundant oxygen defects as highly efficient water oxidation electrocatalyst. *Int. J. Hydrogen. Energy.* **2020**, *45*, 22808-16. DOI
37. Kim, C.; Park, S. O.; Kwak, S. K.; Xia, Z.; Kim, G.; Dai, L. Concurrent oxygen reduction and water oxidation at high ionic strength for scalable electrosynthesis of hydrogen peroxide. *Nat. Commun.* **2023**, *14*, 41397. DOI PubMed PMC
38. Wei, Z.; Wang, H.; Zhang, C.; Xu, K.; Lu, X.; Lu, T. Reversed charge transfer and enhanced hydrogen spillover in platinum nanoclusters anchored on titanium oxide with rich oxygen vacancies boost hydrogen evolution reaction. *Angew. Chem. Int. Ed.* **2021**, *60*, 16622-7. DOI
39. Huang, H.; Huang, A.; Liu, D.; et al. Tailoring oxygen reduction reaction kinetics on perovskite oxides via oxygen vacancies for low-temperature and knittable Zinc-air batteries. *Adv. Mater.* **2023**, *35*, e2303109. DOI PubMed
40. Shao, Z.; Zhu, Q.; Sun, Y.; et al. Phase-reconfiguration-induced NiS/$NiFe_2O_4$ composite for performance-enhanced Zinc-air batteries. *Adv. Mater.* **2022**, *34*, e2110172. DOI PubMed
41. Lepre, E.; Heske, J.; Nowakowski, M.; et al. Ni-based electrocatalysts for unconventional CO_2 reduction reaction to formic acid. *Nano. Energy.* **2022**, *97*, 107191. DOI
42. Choi, C. H.; Kim, M.; Kwon, H. C.; et al. Tuning selectivity of electrochemical reactions by atomically dispersed platinum catalyst. *Nat. Commun.* **2016**, *7*, 10922. DOI PubMed PMC
43. Kim, H. W.; Ross, M. B.; Kornienko, N.; et al. Efficient hydrogen peroxide generation using reduced graphene oxide-based oxygen reduction electrocatalysts. *Nat. Catal.* **2018**, *1*, 282-90. DOI
44. Sa, Y. J.; Kim, J. H.; Joo, S. H. Active edge-site-rich carbon nanocatalysts with enhanced electron transfer for efficient electrochemical hydrogen peroxide production. *Angew. Chem. Int. Ed.* **2019**, *58*, 1100-5. DOI PubMed
45. Lei, X.; Tang, Q.; Zheng, Y.; et al. High-entropy single-atom activated carbon catalysts for sustainable oxygen electrocatalysis. *Nat. Sustain.* **2023**, *6*, 816-26. DOI
46. Tian, Q.; Jing, L.; Du, H.; et al. Mesoporous carbon spheres with programmable interiors as efficient nanoreactors for H_2O_2 electrosynthesis. *Nat. Commun.* **2024**, *15*, 983. DOI PubMed PMC
47. Zhi, Q.; Jiang, R.; Yang, X.; et al. Dithiine-linked metalphthalocyanine framework with undulated layers for highly efficient and stable H_2O_2 electroproduction. *Nat. Commun.* **2024**, *15*, 678. DOI PubMed PMC
48. Tian, Y.; Li, M.; Wu, Z.; et al. Edge-hosted atomic Co-N_4 sites on hierarchical porous carbon for highly selective two-electron oxygen reduction reaction. *Angew. Chem. Int. Ed. Engl.* **2022**, *61*, e202213296. DOI PubMed PMC

Disclaimer/Publisher's Note: All statements, opinions, and data contained in this publication are solely those of the individual author(s) and contributor(s) and do not necessarily reflect those of OAE and/or the editor(s). OAE and/or the editor(s) disclaim any responsibility for harm to persons or property resulting from the use of any ideas, methods, instructions, or products mentioned in the content.

© The Author(s) 2026. Open Access This article is licensed under a Creative Commons Attribution 4.0 International License (https://creativecommons.org/licenses/by/4.0/), which permits unrestricted use, sharing, adaptation, distribution and reproduction in any medium or format, for any purpose, even commercially, as long as you give appropriate credit to the original author(s) and the source, provide a link to the Creative Commons license, and indicate if changes were made.